UN microspheres embedded in UO2 matrix: an innovative accident tolerant fuel

Ribeiro Costa, Diogo; Hedberg, Marcus; Middleburgh, Simon; Wallenius, Janne; Olssen, Par; Lopes, Denise Adorno

Journal of Nuclear Materials

DOI:
10.1016/j.jnucmat.2020.152355

Published: 01/11/2020

Publisher's PDF, also known as Version of record

Journal of Nuclear Materials 540 (2020) 152355

Contents lists available at ScienceDirect

Journal of Nuclear Materials

journal homepage: www.elsevier.com/locate/jnucmat

UN microspheres embedded in UO_2 matrix: An innovative accident tolerant fuel

Diogo Ribeiro Costa [a, b, *], Marcus Hedberg [c], Simon C. Middleburgh [d], Janne Wallenius [a], Pär Olsson [a], Denise Adorno Lopes [b]

[a] KTH Royal Institute of Technology, Nuclear Engineering, 106 91, Stockholm, Sweden
[b] Westinghouse Electric Sweden AB, 721 63, Västerås, Sweden
[c] Chalmers University of Technology, Nuclear Chemistry, 412 96, Goteborg, Sweden
[d] Bangor University, Nuclear Futures Institute, Bangor, Gwynedd, LL57 1UT, UK

ARTICLE INFO

Article history:
Received 17 April 2020
Received in revised form
24 June 2020
Accepted 24 June 2020
Available online 3 July 2020

ABSTRACT

Uranium nitride (UN)-uranium dioxide (UO_2) composite fuels are being considered as an accident tolerant fuel (ATF) option for light water reactors. However, the complexity related to the chemical interactions between UN and UO_2 during sintering is still an open problem. Moreover, there is a lack of knowledge regarding the influence of the sintering parameters on the amount and morphology of the α-U_2N_3 phase formed. In this study, a detailed investigation of the interaction between UN and UO_2 is provided and a formation mechanism for the resulting α-U_2N_3 phase is proposed. Coupled with these analyses, an innovative ATF concept was investigated: UN microspheres and $UO_{2.13}$ powder were mixed and subsequently sintered by spark plasma sintering. Different temperatures, pressures, times and cooling rates were evaluated. The pellets were characterised by complementary techniques, including XRD, DSC, and SEM-EDS/WDS/EBSD. The UN and UO_2 interaction is driven by O diffusion into the UN phase and N diffusion in the opposite direction, forming a long-range solid solution in the UO_2 matrix, that can be described as $UO_{2-x}N_x$. The cooling process decreases the N solubility in $UO_{2-x}N_x$, causing then N redistribution and precipitation as α-U_2N_3 phase along and inside the UO_2 grains. This precipitation mechanism occurs at temperatures between 1273 K and 973 K on cooling, following specific crystallographic grain orientation patterns.

1. Introduction

Uranium dioxide (UO_2) and zirconium-based (Zr) cladding are currently used as standard nuclear fuel and cladding within light water reactors (LWRs). Nevertheless, after the Fukushima Daiichi accident in 2011, the international nuclear community has strived to engineer a successor to the current UO_2–Zr fuel-cladding system, which has been shown to degrade rapidly in such a severe accident scenario [1]. Many studies have been carried out aiming to improve the passive safety of the nuclear fuel system by using accident tolerant fuel (ATF) materials. These new concepts for fuel must maintain or enhance fuel performance under normal and transient operating conditions, as well as during a potential design basis accident (DBA) and beyond-design basis accident (BDBA) [2].

Among many ATF candidates to substitute UO_2 in LWRs, uranium nitride (UN) has been considered as the most promising fuel, mainly owing to its higher uranium density, thermal conductivity, and similar melting point in comparison with UO_2 [3]. Due to its high thermal conductivity, the cooler UN pellet is expected to have lower fission gas release during normal operation [4]. These improved properties also contribute to lower centreline temperature during operation, providing higher margin for melting. Moreover, an increased fission density enables higher burnup, larger power uprates, and an increase in fuel residence time [5–7]. UN fuel pellets have been fabricated by sintering the UN powder [8] using different methods, such as: conventional sintering [9], hot press sintering [10], and spark plasma sintering (SPS) [11]. Additionally, the sol-gel method can be used to fabricate UN microspheres and, then, the UN pellet via SPS [8].

* Corresponding author. KTH Royal Institute of Technology, AlbaNova University Centre, Division of Nuclear Engineering, Roslagsvägen 30 B, 106 91, Stockholm, Sweden.
E-mail addresses: diogorc@kth.se, diogo.drc@hotmail.com (D.R. Costa).

https://doi.org/10.1016/j.jnucmat.2020.152355

One major drawback in using the UN as a fuel in LWR is its low oxidation resistance when in contact with the coolant water [12]. In this situation, the UN readily loses its structural integrity, reacts exothermically and, consequently, results in fuel pellet pulverisation, oxidation, washout and relocation. Other studies have shown that the UN fuel also loses its integrity when in contact with air, submerged water, superheated steam, and H_2O_2 [13–17].

In order to overcome the technical challenges of using the UN as LWR fuel, its resistance to water corrosion has to be improved. To do so, composite fuel designs have been proposed to mitigate this detrimental behaviour. The fundamental idea of such composite fuels is to combine a material, with a better oxidation resistance, with the UN fuel forming a barrier layer to prevent the UN oxidation. Some materials have already been studied: USi_x, CrN and AlN [18], ZrN [19], U_2Si_3 [20,21], and UO_2 [9,10,22]. Among these materials, the UO_2 has important advantages since it is already used as standard nuclear fuel in LWR, as well as it has a good oxidation resistance against water. Thus, the combination of UO_2 and UN should result in a UN-UO_2 composite fuel with improved oxidation resistance (UO_2 contribution), as well as improved uranium density and thermal conductivity (UN contribution). In fact, Yang et al. [10] showed that the combination of UN (70 wt%) and UO_2 increased the uranium density by 13% (10.91 g/cm^3) and the thermal conductivity up to 100% (8.16 W/m.K at 1073 K), in comparison with pure UO_2. Additionally, Shivprasad et al. [23] presented isothermal corrosion studies of UN(5–30 vol%)-UO_2 composite fuels at 623 K, under 82% steam for 12 h. The addition of uranium dioxide significantly delayed the onset temperature of oxidation. Therefore, there is a potential application of UN-UO_2 composite fuels for use in LWRs.

However, the complexity related to the interaction between the UN and the UO_2 fuels during sintering is still an open problem of interest. A previous study [9] mixed UO_2 (5–10 wt%) and UN powders in a high energy planetary ball mill, and sintered the mixtures at 1973–2273 K in Ar-100 ppm N_2. Higher sintering temperatures resulted in lower sintered densities, attributed to a preferential formation of oxygen-stabilised hyper-stoichiometric nitrides (UN_{1+x}) or uranium oxynitrides phases. Other previous work [10] used hot pressing sintering (1573–1863 K, vacuum) to fabricate UN (30–70 wt%)-UO_2 composites. A new phase, α-U_2N_3 (sesquinitride), was identified in the sintered composites by XRD analyses. In this work, Yang et al. suggested that this sesquinitride phase might be originated from the $U(ON)_{2-x}$ type oxynitride phase during cooling. Malkki [19] also suggested the formation of this sesquinitride phase in the UN pellet, specifically in the UO_2 inclusions (impurity). The explanations were based on either an incomplete denitriding of the sesquinitride powder during fabrication, or on oxygen and carbon impurities presented in the UN powder that "knocked-out" the nitrogen atoms from its lattice, allowing them to diffuse further into the UN bulk to form the U_2N_3. Recently, Mishchenko [22] mixed crushed UN pellet (125–335 μm and 335–1000 μm) with stoichiometric UO_2 powder and sintered the mixtures at 1673 K and 1873 K, using SPS in vacuum. Nitrogen was observed to be very mobile in the UO_2 matrix, forming a secondary nitride phase along the UO_2 grain boundaries. After the annealing experiments (1873 K, 20 h, Ar), the sesquinitride (U_2N_3) was found and its formation was proposed to occur during the cooling stage when the temperature dropped to approximately 1073 K.

The presented literature related to a formation mechanism of the α-U_2N_3 phase is limited, divergent, and does not address its physical localisation in the UN-UO_2 microstructure. Moreover, there is a lack of knowledge in how the sintering parameters impact the amount and morphology of the sesquinitride phase. This phase may be detrimental to the fuel performance, since it dissociates in uranium nitride and nitrogen upon heating in reduced nitrogen conditions. At high temperatures and irradiation, the nitrogen evolution during the decomposition would not only increase the fuel pin pressure and result in undesirable cladding embrittlement, but also would cause additional cracks in the fuel during irradiation [24]. Therefore, a detailed study to understand the main influence of the sintering parameters on the interaction between UN and UO_2, as well as on the formation mechanism of the α-U_2N_3 phase, becomes quite important to minimise (or avoid) the α-U_2N_3 formation.

In the present work, a detailed investigation of the interaction between UN and UO_2 during sintering is presented. An innovative ATF concept was used for this purpose: mixtures of UN microspheres and hyper-stoichiometric $UO_{2.13}$ powder were sintered by SPS at different temperatures, applied pressures, times and cooling rates. This work also describes the influence of the SPS processing parameters on the amount and morphology of phases after sintering. Therefore, future works will be able to fabricate a high density UN-UO_2 composite fuel and minimise (or avoid) the sesquinitride formation during sintering.

2. Methods

2.1. Raw materials

The uranium dioxide (UO_2) powder used in this study was supplied by Westinghouse Electric Sweden AB, and was reported to have O/U ratio of 2.13, fill density of 2.19 g/cm^3, specific surface area of 5.33 m^2/g, mean particle size of 20.20 μm, and 900 ppm of H_2O as the main contaminant. The H_2O content was determined by the Karl Fisher titration method.

The uranium nitride microspheres (UN) were fabricated at Chalmers University of Technology by the internal sol-gel process, which consisted of three main steps: the internal gelation, the microsphere conversion to oxide, and the carbothermic reduction [8]. Fig. 1 summarises the thermal processes used in the conversion and carbothermic steps. The as-fabricated UN microspheres contained 5.71 wt% of N, 833 ppm of carbon, and 1010 ppm of oxygen. N and O analyses were performed by the inert fusion method, using a LECO TC436DR equipment inside a nitrogen-filled glove box to minimise oxygen incorporation during sample preparation and analyses. The UN microspheres were kept under argon for the duration of the investigations.

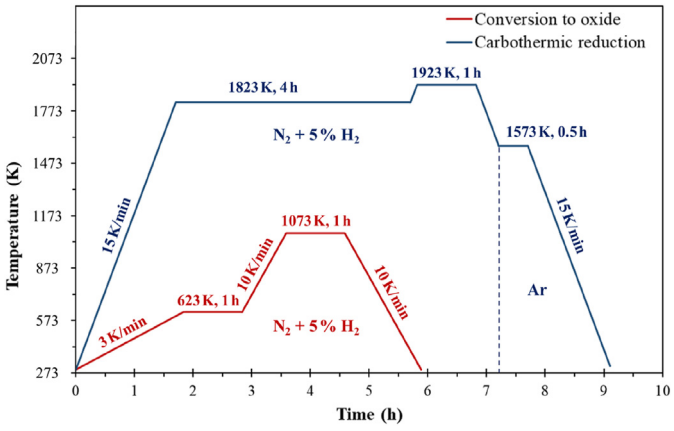

Fig. 1. Thermal processes used for the microsphere conversion to oxide (red) and for the carbothermic reduction (blue). Argon was used from 1573 K on cooling to avoid U_2N_3 formation. (For interpretation of the references to colour in this figure legend, the reader is referred to the Web version of this article.)

2.2. Sample preparation and fabrication

Pure $UO_{2.13}$ powder, pure UN microspheres, and mixtures of 10, 30 and 50 wt% of UN microspheres and $UO_{2.13}$ powder were sintered by the spark plasma sintering (SPS) method at the National SPS Facility in Stockholm/Sweden. The SPS equipment is a modified Dr. Sinter SPS machine inside a glove box, under argon atmosphere (<0.1 ppm O_2), to avoid oxidation during preparation and sintering. Mixtures of $UO_{2.13}$ powder and the as-fabricated UN microspheres (without crushing or pulverisation) were prepared inside a glove box connected to the SPS. Before each sintering, the mixtures (~4 g each) were manually homogenised in a small beaker (25 mL) for 1 min with a spatula, and then poured out in a die and transferred to the SPS chamber. A graphite die with 9.50 mm inner diameter was used to sinter the materials, along with two graphite punches and a thin graphite paper to protect the samples, the punches, and the inner die surface from undesirable interaction during sintering. The outer surface of the die was wrapped with three sheets of graphite felt to reduce the heat loss from the graphite surface, as well as to decrease the thermal gradient between the pellet and the outer surface of the die. A circular window of about 10 mm in diameter was cut into the felt to allow temperature measurements, on the die outer surface, by using a pyrometer during the sintering. The lower limit of detection of the pyrometer was 673 K, therefore the heating programs were initiated after the die surface temperature reached this value.

The sintering chamber of the SPS machine was loaded with the entire die assembly and depressurised to about 2 Pa. A number of parameters were monitored as a function of time during the sintering process, including: die wall temperature, applied uniaxial pressure, total z-axis displacement of the punches (shrinkage), vacuum line pressure, current, and voltage. In this study, the die wall temperature, which is slightly lower than the centreline temperature of the samples inside the die, is considered to be the "sintering temperature" of the experiments. Additionally, the total z-displacement included the elastic and thermal deformations of the material, combining the effects of temperature, applied pressure, and amount of sample. Materials were sintered at different temperatures, applied pressures, holding times and cooling rates to evaluate the main influence of each parameter on the sintering behaviours and sintered densities, as well as on the final microstructures. Table 1 presents the SPS parameters used and the sample identification.

The samples are named in this study as follows: UN(X)-UO_2 (T/P/t/SC or FC), where "X" is the amount of UN microspheres in weight percent (wt%), "T" is the sintering temperature, "P" is the applied pressure during the sintering, and "SC/FC" are the slow cooling (SC) and fast cooling (FC) rates, respectively. For instance, the sample UN(30)-UO_2 (1373/80/3/SC) is related to a mixture of 30 wt% of UN microspheres and 70 wt% of $UO_{2.13}$ powder, sintered at T = 1373 K and P = 80 MPa, during t = 3 min at 1373 K, and using a slow cooling rate from 1373 K (SC) until room temperature. The heating rates were kept constant at 100 K/min until 1373 K (or 1573 K), and then 50 K/min until 1373 K (or 1773 K).

After the sintering processes, the pellets were removed from the graphite die and prepared for characterisation. This preparation consisted of removing all the residual graphite material by grinding the external surface of the sintered samples with SiC paper (grit 280).

2.3. Characterisation

The uranium dioxide powder and UN microspheres were characterised using scanning electron microscopy (SEM) and X-ray diffraction (XRD) to assess the morphologies and crystalline structures, respectively. The SEM used was a SEM FEI XL30 with the INCA software. The external surfaces of both materials were examined using the secondary electrons (SE) detector. The UN microspheres' bulk morphologies were also examined after standard metallographic preparation (grinding and polishing) of spheres that were hot mounted in a phenolic resin with carbon filler. The average density, considering a perfect sphere shape, was calculated based on the average diameter of 35 microspheres, with 4 measurements per microsphere (140 measurements in total), and the average weight (65 microspheres).

The XRD scans of both materials were performed using a Siemens D5000 diffractometer with a $Cu_{K\alpha}$ radiation (Ni filter), 2θ ranging between 20° and 120°, with 2θ step of 0.02° and acquisition time of 9 s for each step. The lattice parameters and crystallite sizes, with their uncertainties, were calculated using the software MAUD (Materials Analysis Using Diffraction) [25], which performs the calculations based on the Rietveld method. Prior to the analyses, the UN microspheres were milled inside a glove box (argon atmosphere) and encapsulated in a special specimen holder for the XRD acquisition (Bruker model A100B138−B141). This holder contains a knife-edge used to provide a high resolution, low background XRD diffraction patterns in an air-tight atmosphere. Its use was very important since the milled UN microsphere is pyrophoric

Table 1
Spark plasma sintering parameters and sample identification.

Material	UN microsphere (wt%)	Temperature (K)	Pressure (MPa)	Time (min)	Cooling rate (K/min)	Sample identification
UO_2 powder	0	1373	40	3	SC_{1373}	UO_2 (1373/40/3/SC)
	0	1373	40	3	FC_{1373}	UO_2 (1373/40/3/FC)
	0	1373	80	3	SC_{1373}	UO_2 (1373/80/3/SC)
	0	1773	40	3	SC_{1773}	UO_2 (1773/40/3/SC)
	0	1773	80	3	SC_{1773}	UO_2 (1773/80/3/SC)
UN microsphere	100	1773	80	3	SC_{1773}	UN (1773/80/3/SC)
UN-UO_2	30	1373	40	3	SC_{1373}	UN(30)-UO_2 (1373/40/3/SC)
	30	1373	80	3	SC_{1373}	UN(30)-UO_2 (1373/80/3/SC)
	30	1373	80	3	FC_{1373}	UN(30)-UO_2 (1373/80/3/FC)
	30	1773	40	3	SC_{1773}	UN(30)-UO_2 (1773/40/3/SC)
	30	1773	80	3	SC_{1773}	UN(30)-UO_2 (1773/80/3/SC)
	30	1773	80	3	FC_{1773}	UN(30)-UO_2 (1773/80/3/FC)
	10	1773	80	3	FC_{1773}	UN(10)-UO_2 (1773/80/3/FC)
	10	1773	80	60	FC_{1773}	UN(10)-UO_2 (1773/80/60/FC)
	50	1773	80	3	FC_{1773}	UN(50)-UO_2 (1773/80/3/FC)

SC = slow cooling rate; FC = fast cooling rate; SC_{1373} = 10 K/min (1373-1173 K) and 20 K/min (1173-973 K); FC_{1373} = 50 K/min (1373-1173 K); SC_{1773} = 10 K/min (1773-1573 K), 20 K/min (1573-1373 K) and 50 K/min (1373-973 K); FC_{1773} = 50 K/min (1773-1173 K); the heating rates were kept constant: 100 K/min until 1273 K (or 1573 K), and then 50 K/min until 1373 K (or 1773 K).

when in contact with air.

Differential scanning calorimetry (DSC) was performed in a Netzsch STA 449 F3 Jupiter equipment under argon (99.999%) atmosphere and oxygen getter (Zr metal). A mixture of 30 wt% UN microspheres and $UO_{2.13}$ powder was processed to evaluate any interaction/reaction between both phases during sintering. The sample was heated at 10 K/min up to 1573 K, kept at this temperature for 30 min, and cooled to room temperature also at 10 K/min under argon atmosphere.

All the sintered samples were characterised after the post-SPS preparation, i.e. grinding the surface to remove the residual graphite foil from the SPS process. The sintered densities were measured using a modified Archimedean method, with chloroform as the immersion medium [11]. The sintered samples were milled to powder in an argon filled glove box and analysed using the same XRD equipment, parameters and holder. The theoretical densities (TD) were calculated based on the weight fractions of each phase after SPS using the Rietveld method and the software MAUD [25]. The reference values [26] for UO_2, UN and α-U_2N_3 were 10.96 g/cm^3, 14.32 g/cm^3 and 11.24 g/cm^3, respectively.

Scanning electron microscopy examinations were performed in a polished longitudinal cross section of each sintered sample, using both secondary and backscattered electron (BSE) detectors. AGAR SEM carbon coater was used to cover the samples with a conducting carbon layer for the SEM analyses. The semi-quantitative chemical characterisation were assessed by means of energy-dispersive X-ray spectroscopy (EDS) and wavelength dispersive spectroscopy (WDS) analytical techniques. All the SEM-SE/BSE analyses were carried out in the same equipment, a SEM FEI XL30 and INCA software. The SEM-EDS/WDS analyses were performed in a field emission gun (FEG) SEM JEOL JSM-7000F. Additionally, electron backscatter diffraction (EBSD) analyses were carried out in a high-resolution FEG SEM-EBSD (Zeiss GeminiSEM450) microscope. A diamond-polished UN-UO_2 sintered pellet for EBSD analyses was chemical-mechanically final polished using an Al-oxide suspension of 0.05 μm (Buhler Masterprep) for about 30 min. The phases and the grain orientations of each phase present in the sample could be assessed.

3. Results and discussion

3.1. Phase and morphology of the raw materials

Fig. 2 reports the phases and morphologies of (a) the UN microsphere and (b) the $UO_{2.13}$ powder, as well as the XRD diffractograms. Pure cubic phases were found in both materials, with very low intensity peaks matching the UO_2 phase (e.g. 28.2° and 32.7°) in UN sample, which were from the oxygen impurity. The calculated lattice parameters/crystallite sizes were 48.873(1) nm (ref. 48.80(5) nm [26])/163(2) nm, and 54.593(5) nm (ref. 54.581(5) nm [26])/53 (1) nm for UN and $UO_{2.13}$, respectively. Both materials had similar lattice parameters when compared to the references values including the error margins. As-fabricated UN microspheres were porous with an average diameter of 847(12) μm, average weight of 2.35 mg, and geometric density (perfect sphere assumption) of 7.40 g/cm^3, which represents about 52% of the theoretical density (TD) [26]. The $UO_{2.13}$ morphology is characteristic of the industrial ammonium uranium carbonate (AUC) wet route [27].

3.2. Interaction between UN and UO_2 during sintering

The applied pressure and the amount of UN microspheres affected the sintering behaviours (shrinkages) of the samples. Fig. 3(a) reports that changes in pressure from 40 MPa to 80 MPa resulted in an early shrinkage for the $UO_{2.13}$ powder, without changing the typical S-shaped curve for uranium dioxide [28–30]. This shift may be attributed to a higher particle-particle contact owing to the higher pressure (80 MPa), which promoted the first stage of sintering and, consequently, the whole sintering process [31]. Fig. 3 (b) shows that the higher the amount of UN microspheres, the higher the sintering blockage. The microspheres acted as obstacles preventing the contact between the $UO_{2.13}$ particles in the initial sintering steps. Similar sintering blockage is observed in the UO_2-Gd_2O_3 [28,30] and UO_2–Cr_2O_3 [32] systems. Pure UN microspheres started shrinking only at (about) 1273 K, and were still sintering at 1773 K. The overshoots in temperature at approximately 653 K were caused by the pyrometer specification, since it started measuring the die temperature just above 673 K.

The pressures in the exhaust line (vacuum system) during sintering at 1773 K and 80 MPa were also monitored and are plotted in Fig. 4. Two peaks appeared during $UO_{2.13}$ sintering: one at low (<673 K) and another at high (~1473 K) temperatures. The first may be due to water desorption and uranyl hydroxides decomposition (e.g. $UO_2(OH)_2.xH_2O$) [33,34]. The second peak (~1473 K) in Fig. 4 is due to oxygen liberation from the hyper-stoichiometric $UO_{2.13}$ powder [35]. Regarding the UN(30)-UO_2 sample, the first peak is also present but the second one disappeared. This indicates that the oxygen from the oxide powder interacted with the UN in some extension, as previously suggested [10]. Pure UN microspheres did not show any significant change in pressure, just a small one at low temperatures (<673 K). The results for 1373 K were equivalent and are not shown in Fig. 4.

The phenomena at low temperatures were investigated by DSC analysis of UN(30)-UO_2 in Ar. Fig. 5 shows three endothermic peaks at about 443 K, 518 K and 658 K. Peres et al. [33] reported peaks at 428 K and 543 K owing to water desorption during thermogravimetric studies of $UO_{2.069}$ powder in H_2-1.47% CO_2. Prince and Stuart [34] performed DSC and infra-red analyses during $UO_2(OH)_2 \cdot H_2O$ decomposition in N_2 and found endothermic peaks related to water elimination at 413 K, and to hydroxyl (OH) dissociation from the oxide at 623 K. Therefore, the increase in pressure at low temperatures (Fig. 4) may be a cumulative result of water desorption and hydroxyl dissociation.

The interaction between oxygen and UN was also investigated by DSC analysis of UN(30)-UO_2 in Ar. Fig. 6 shows a broad exothermic peak at about 1188 K and a smaller one at about 1458 K, which is quite close to the maximum release of oxygen presented in Fig. 4 (1473 K). These exothermic peaks confirm that the interaction between oxygen and UN started at about 1098 K and continued until 1573 K, coherently with the SPS results in Fig. 4.

3.3. Phases, compositions and densities after sintering

Typical SEM-BSE images of UN microspheres embedded in UO_2 are present in Fig. 7 (a,b) (lower magnification) and Fig. 7 (c,d) (higher magnification). The interface between the dense UO_2 matrix (point P1) and the porous UN microsphere region (point P2) is highlighted by a dashed line in Fig. 7 (d). Precipitates were formed in the UO_2 matrix and are indicated by arrows. These precipitates, highlighted in Fig. 7 (d), were spread throughout the pellet.

As reported in Fig. 7 (a,b), the embedded microspheres deviate from a spherical shape to a more elongated and irregularly shaped phase. This phenomenon may be a result of the compressive stress applied combined with the heating process in SPS, since the heated material is able to undergo plastic deformation and densification under the uniaxial load [36,37].

SEM-EDS chemical maps of N, U and O were performed and the results are shown in Fig. 8. From the N chemical map, the precipitates in the UO_2 matrix are a nitrogen-rich phase compound

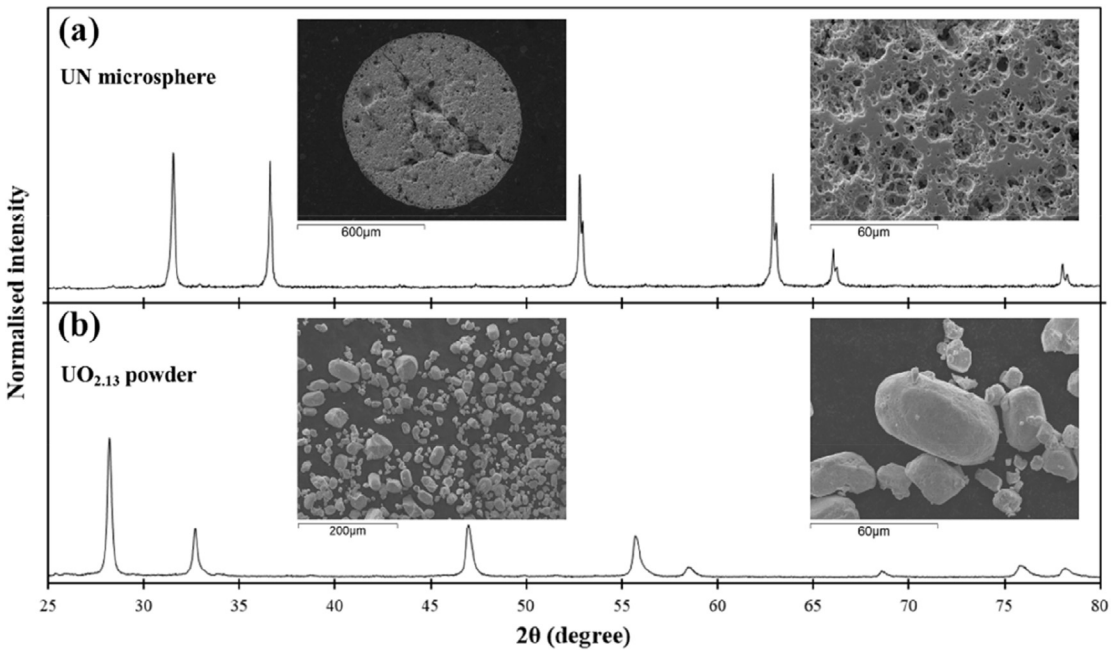

Fig. 2. X-ray diffraction patterns of (a) the UN microsphere and (b) the $UO_{2.13}$ powder. Insets in (a) show cross section images of an as-fabricated porous UN microsphere, and insets in (b) show a characteristic morphology of $UO_{2.13}$ powder ex-AUC [27]. Low intensity peaks matching the UO_2 phase (e.g. 28.2° and 32.7°), originated from the oxygen impurity, are present in diffractogram (a).

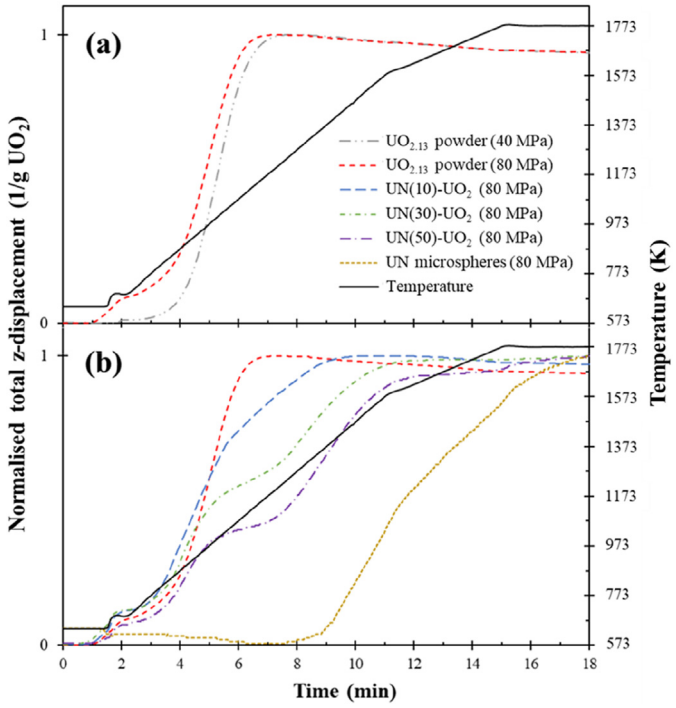

Fig. 3. Sintering behaviours (shrinkage) of samples sintered at 1773 K showing (a) the normalised curves for $UO_{2.13}$ sintered at 40 MPa and 80 MPa, (b) the influence of UN microsphere (0–100 wt%) addition on the shrinkage curves. Higher pressure favoured the sintering, and the higher the UN additions the stronger the sintering blockage.

with a long range lamellar-type shape structure. The O chemical map shows the oxide phase, and the U content map mainly shows the pores but also shows slight changes in U density (brighter in the N-rich regions). The oxide layer inside the UN microsphere is a result of the interactions between UO_2 and UN during sintering (details are described in section 3.4). Previous works also found a nitrogen-rich phase in studies related to UN with UO_2 impurities [19] and UN-UO_2 composite fuels [22].

To identify the phases, semi-qualitative SEM-EDS measurements were performed at the point P1, as well as SEM-EDS/WDS at the points P2 and P3 in Fig. 7. Table 2 reports the results, in atomic percent (at%), of oxygen, nitrogen, and uranium contents. The EDS values for point P1 are in agreement with the UO_2 phase. EDS/WDS results for point P3 showed that the nitrogen contents were ~64 at% (EDS) and ~51 at% (WDS), and for point P2 the values were ~53 at% (EDS) and ~42 at% (WDS), both lower than those at P3. Therefore, the phase P3 has a higher N/U ratio than the phase at P2, which indicates that the precipitates formed are the α-U_2N_3 phase (sesquinitride). Consequently, the point P2 represents the UN phase.

SEM-EBSD analysis was carried out to corroborate the information obtained from EDS and WDS analyses. The colour phase map of some precipitates is presented in Fig. 9 (right side), demonstrating that the precipitates are the α-U_2N_3 phase (cubic structure, 106.99 nm, Laue group 10, $Ia\bar{3}$). As expected, the red coloured phase is related to the UO_2 matrix (cubic structure, 54.65 nm, Laue group 225, $Fm\bar{3}m$).

The powder XRD analyses presented in Fig. 10 confirmed that the α-U_2N_3 phase (ICSD PDF 00-015-0426) appeared in all composites. A standard mixture of $UO_{2.13}$ and UN microspheres (30 wt %) powders was used as the reference phases for UO_2 and UN, respectively. Previous studies proposed or identified this sesquinitride phase in sintered samples [9,10,19,22], but have not specifically addressed its physical localisation as we presented in this study.

Cooling rate, temperature and pressure affected the weight fractions (wt%) of each phase after sintering, but the sintering time did not impact the amounts significantly. The results in Fig. 11 reports that the faster the cooling, the higher the amount of UN and the lower the amount of α-U_2N_3. Comparing the samples UN(30)-UO_2 (1373/80/3/SC) and UN(30)-UO_2 (1373/80/3/FC), for instance, the UN content increased from 10.3 ± 0.2 wt% to 13.3 ± 0.5 wt%, and

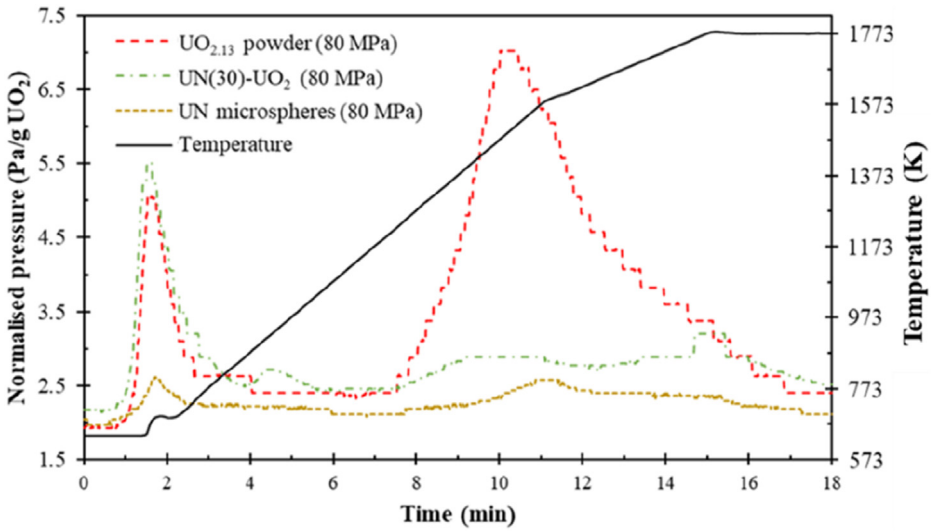

Fig. 4. Variation of the normalised vacuum pressure during the sintering (1773 K, 80 MPa) of pure $UO_{2.13}$ powder, UN(30)-UO_2 composite fuel, and pure UN microspheres. Low temperature peaks (<673 K) may be due to water desorption and uranyl hydroxides decomposition (e.g. $UO_2(OH)_2.xH_2O$) [33,34], and high temperature peak (~1473 K) to oxygen elimination from the hyper-stoichiometric $UO_{2.13}$ powder [35]. For the sample UN(30)-UO_2, the peak at (about) 1473 K disappeared, indicating that the oxygen from the oxide powder interacted with the UN.

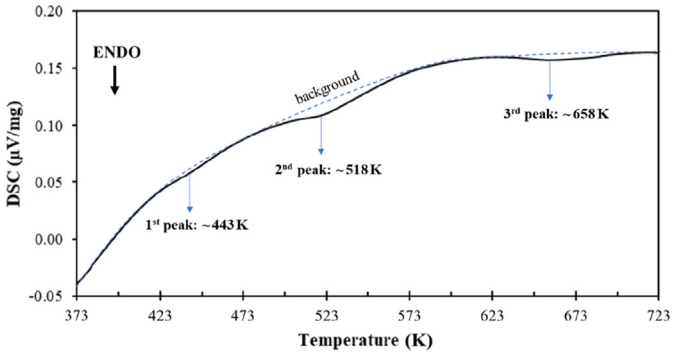

Fig. 5. Differential scanning calorimetry analysis of a UN(30)-UO_2 composite as a function of temperature. Endothermic peaks (ENDO) are pointed downwards from the background (dashed line). The three endothermic peaks are related to water desorption (1st and 2nd) and hydroxyl (HO) elimination (3rd) [33,34].

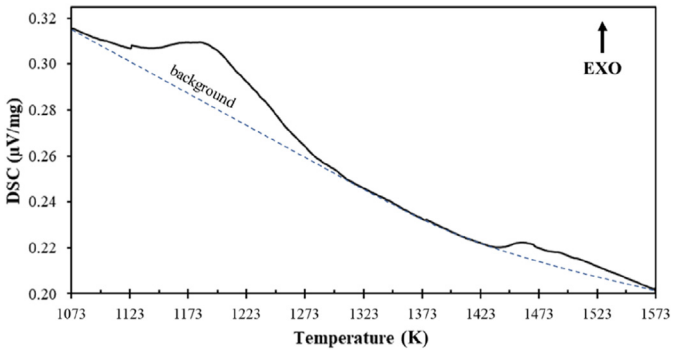

Fig. 6. Differential scanning calorimetry analysis of a UN(30)-UO_2 composite as a function of temperature. Exothermic peaks (EXO) are pointed upwards from the background (dashed line). The two exothermic peaks are related to the O interaction with the UN microspheres.

the amount of α-U_2N_3 decreased from 15.1 ± 0.7 wt% to 12.7 ± 0.7 wt% when the system was cooled faster. Temperature and pressure followed the same trend: the higher the temperature (or pressure), the higher the amount of α-U_2N_3 and the lower the amount of UN. As previously discussed with the data provided in Fig. 3, the increase in pressure resulted in an early volume reduction of the material and, consequently, the system reached the sintering regime faster. A previous study [10] used the hot press sintering method to sinter a mixture of 30 wt% of UN and UO_2 powders. The authors found that the weight fractions of UN and α-U_2N_3 increased and decreased, respectively, by increasing the sintering temperature from 1573 K to 1773 K. This different behaviour might be related to the semi-quantitative method used to determine the weight fraction of the phases and/or some small variation on cooling.

Fig. 11 also reports that the temperature impacted the sintered densities (%TD). Samples sintered at 1373 K showed densities between 88.3 %TD and 89.9 %TD. At 1773 K, the densities increased to (about) 91–96 %TD, with the highest value of 95.6 %TD in sample UN(30)-UO_2 (1773/80/3/SC). A previous study [9] in UN-UO_2 (10 wt %) composite fuel showed that a maximum sintered density of 94 % TD was obtained at 1973 K during 5 h using conventional sintering, under Ar-100 ppm N_2 atmosphere. Another study [10] obtained almost fully dense composite pellets (30–70 wt% of UN + UO_2) using hot press sintering at 1773 K for 4 h in vacuum. These two previous papers show that the sintering method is crucial to obtain a high density UN-UO_2 pellet. Indeed, our study demonstrated that is possible to obtain high density composite fuels, e.g. 95.6 %TD, using the SPS method with quite short sintering time (3 min). The values for pure UO_2 samples are omitted from Fig. 11 since the changes in SPS parameters did not affect the sintered densities (% TD) significantly: the values ranged from 97.5 %TD to 98.9 %TD. In comparison to conventional sintering, which requires high temperatures and long sintering times to obtain high density pellet (2033 K, 5.7 h, 97.2 %TD) [38], the SPS technique is much faster and efficient for research and development.

3.4. Formation mechanism of the α-U_2N_3 phase

The size and morphology of the α-U_2N_3 precipitates are significantly affected by temperature (Fig. 12) and cooling rate (Fig. 13). Fig. 12 (top images) reports SEM-BSE images of sample UN(30)-UN

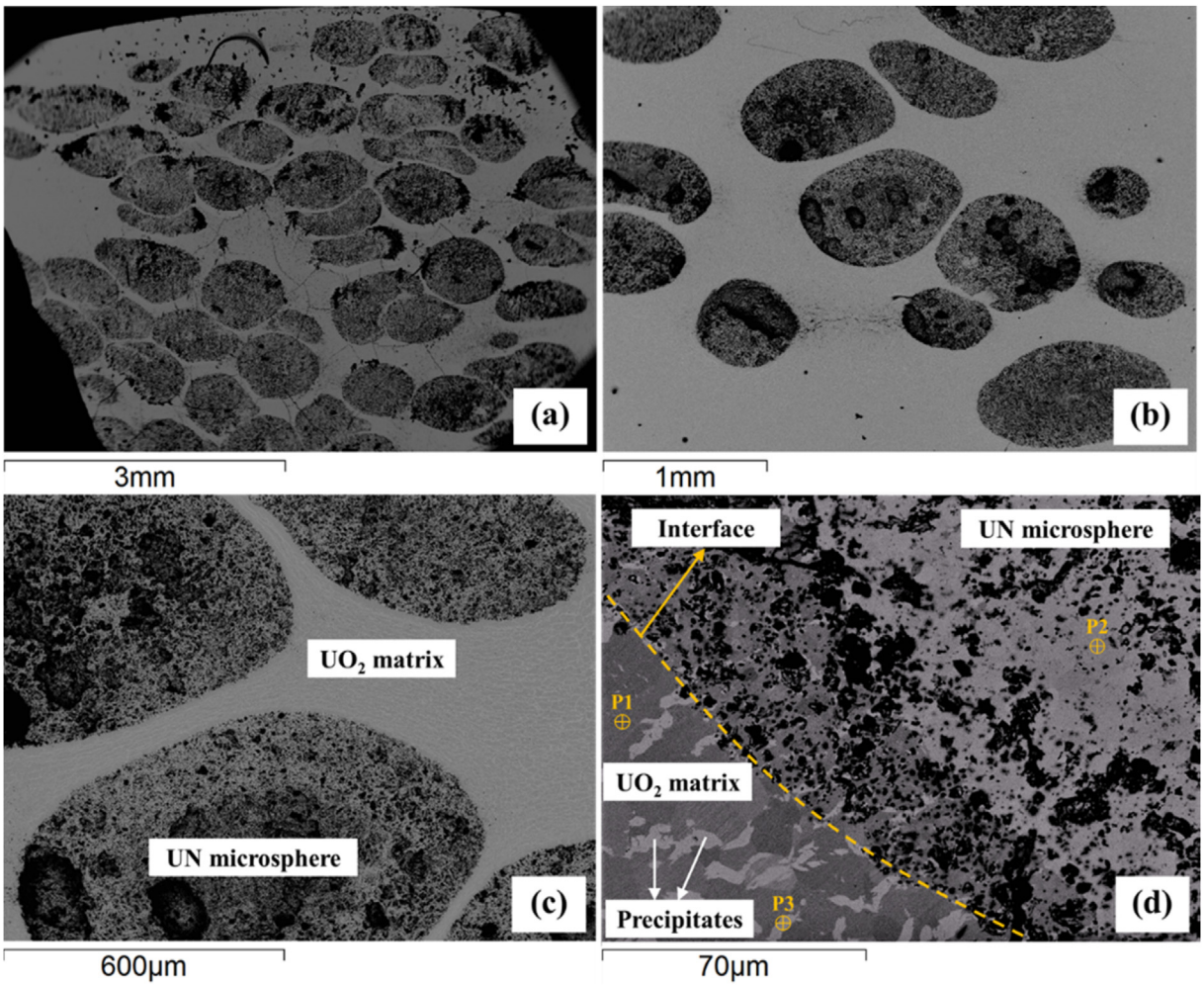

Fig. 7. SEM-BSE images of UN microspheres embedded in UO_2 matrix at lower magnification (a,b), and higher magnification (c,d), highlighting the interface (dashed line) between the UO_2 phase (point P1) and the UN microsphere (point P2), as well as the precipitates formed after sintering (point P3). The precipitates, highlighted in Fig. 7 (d), were spread throughout the pellet.

(1373/80/3/SC), showing that the precipitates are much finer than the ones of sample UN(30)-UN (1773/80/3/SC) (bottom images in Fig. 12). Additionally, the α-U_2N_3 phase at 1373 K is formless when compared to the precipitates at 1773 K. From the images at 1773 K, the long range lamellae have in average thickness of ~4 μm and are ~15 μm long and often bridged/connected with each other. At 1373 K, the dispersed and much finer precipitates have an average size of few microns (~1–2 μm) with a quasi-lamellar-type structure, which is correlated with some porosity along the structure (see the highest magnification image). It seems that when the α-U_2N_3 formed in the UO_2 matrix, e.g. during the sintering at 1373 K, some pores were also formed. This phenomenon may be related to a volume shrinkage during the nitride formation, since its density is higher than the oxide phase [26]. A recent study also found this correlation between porosity and nitride phase formation in UO_2 matrix [22]. Since the pressure did not significantly affect the size and morphology of the precipitates, only their amount, the results for 40 MPa are omitted in Figs. 12 and 13. As discussed in sections 3.2 and 3.3, a higher applied pressure results in a greater amount of α-U_2N_3 formed. The composites sintered at 80 MPa were exposed to a longer time at higher temperatures (close to the sintering temperatures) compared to the 40 MPa samples, allowing then extra diffusion of N and O throughout the pellet (more details are presented in this section).

Fig. 13 reports the cooling rate effect on the size and morphology of the precipitates. SEM-BSE images of UN(30)-UN (1773/80/3/SC) and UN(30)-UN (1773/80/3/FC) are presented in Fig. 13 (top) and Fig. 13 (bottom), respectively. As described in Table 1, the slow cooling rate (SC) profile adopted was: 10 K/min (1773-1573 K), 20 K/min (1573-1373 K) and 50 K/min (1373-973 K). From 973 K on, the cooling held naturally, i.e. no control over the cooling rate was applied. The fast cooling (FC) profile was: 50 K/min (1773-1173 K), followed by natural cooling after 1173 K. Consequently, the SC and FC duration, from 1773 K to 973 K, were about 38 min and 13 min, respectively. Sample UN(30)-UN (1773/80/3/SC) had a long range lamellar-type structure after slow cooling from 1773 K. However, in the fast cooled sample, the size and morphology of the precipitates drastically changed from lamellae to a “coarse grain” structure, with various sizes (~5 μm–35 μm). These microstructures are characteristic of a precipitation mechanism [39], in which the nitrogen has to be redistributed since its solubility in UO_2 decreases with the decrease in temperature [40]. Thus, the faster the cooling, the lower the N redistribution time into the UO_2 matrix and, consequently, less homogeneous the structure.

DSC analysis was performed to identify when the precipitates started forming. Fig. 14 shows a DSC curve of a cooling step (10 K/min) containing a broad exothermic peak between (about) 1253 K and 998 K, indicating a precipitation reaction [41]. Thus, the N

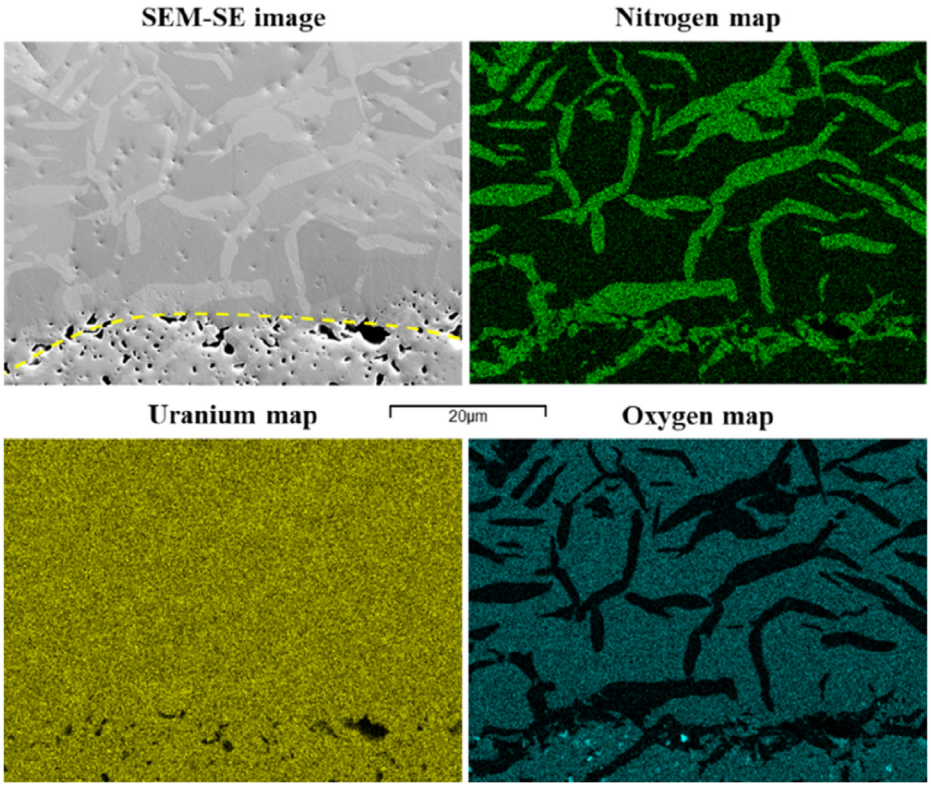

Fig. 8. EDS chemical maps of a composite fuel showing distinct nitrogen and oxygen-rich regions. The nitrogen map shows a N-rich phase compound with a long range lamellar-type shape structure. The interface between the embedded UN microsphere and the UO_2 matrix is highlighted by a dashed line. The oxide layer inside the UN microsphere is a result of the interactions between UO_2 and UN during sintering (details are described in section 3.4).

Table 2
EDS and WDS semi-quantitative analyses of oxygen, nitrogen and uranium contents (at%) at the points P1 (UO_2 matrix), P2 (UN microsphere) and P3 (precipitate) marked in Fig. 7.

Point analysis (position)	Oxygen content (at%)		Nitrogen content (at%)		Uranium content (at%)	
	EDS	WDS	EDS	WDS	EDS	WDS
P1 (UO_2 matrix)	67.7	n.m.	n.d.	n.m.	32.3	n.m.
P2 (UN microsphere)	10.3	8.6	53.0	42.0	36.7	49.4
P3 (precipitate)	8.1	9.9	63.7	50.6	28.1	39.5

n.d. = not detected; n.m. = not measured.

redistribution seems to occur within the temperature range of 1273 K−973 K on cooling.

Therefore, the formation mechanism of the α-U_2N_3 phase may be explained by the interdiffusion of O and N during the heating step of sintering, followed by a precipitation phenomenon during the cooling step. Fig. 15 (a,b) show low magnification SEM-BSE images of UN microspheres embedded in UO_2 matrix, as well as the α-U_2N_3 phase (brighter phase) spread throughout the pellet. Fig. 15 (c) illustrates the proposed formation mechanism using a SEM-BSE image of UN(30)-UN (1373/80/3/SC). The dashed line highlighted the interface between the UO_2 matrix and the UN

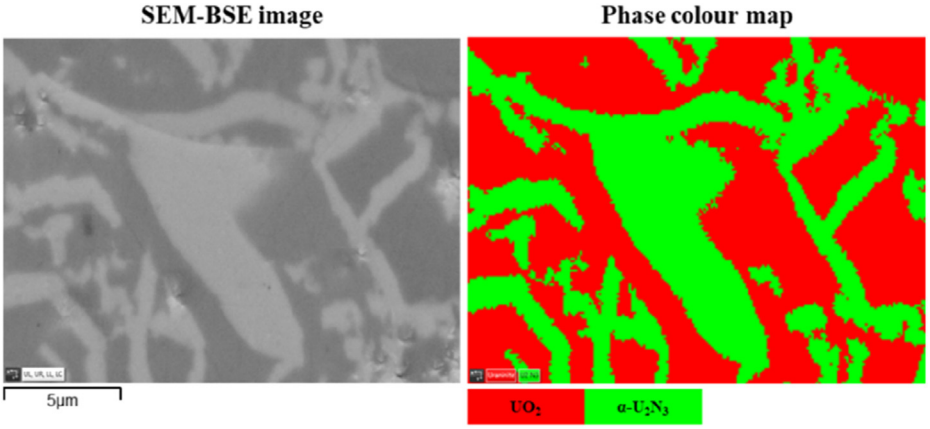

Fig. 9. EBSD phase colour map (right side) of a SEM-BSE image (left side) containing the UO_2 matrix (darker region) (cubic structure, 54.65 nm, $Fm\bar{3}m$, Laue group 225) and the precipitates (brighter region). The colour map confirms that the precipitates are the α-U_2N_3 phase (green colour) (cubic structure, 106.99 nm, $Ia\bar{3}$, Laue group 10). (For interpretation of the references to colour in this figure legend, the reader is referred to the Web version of this article.)

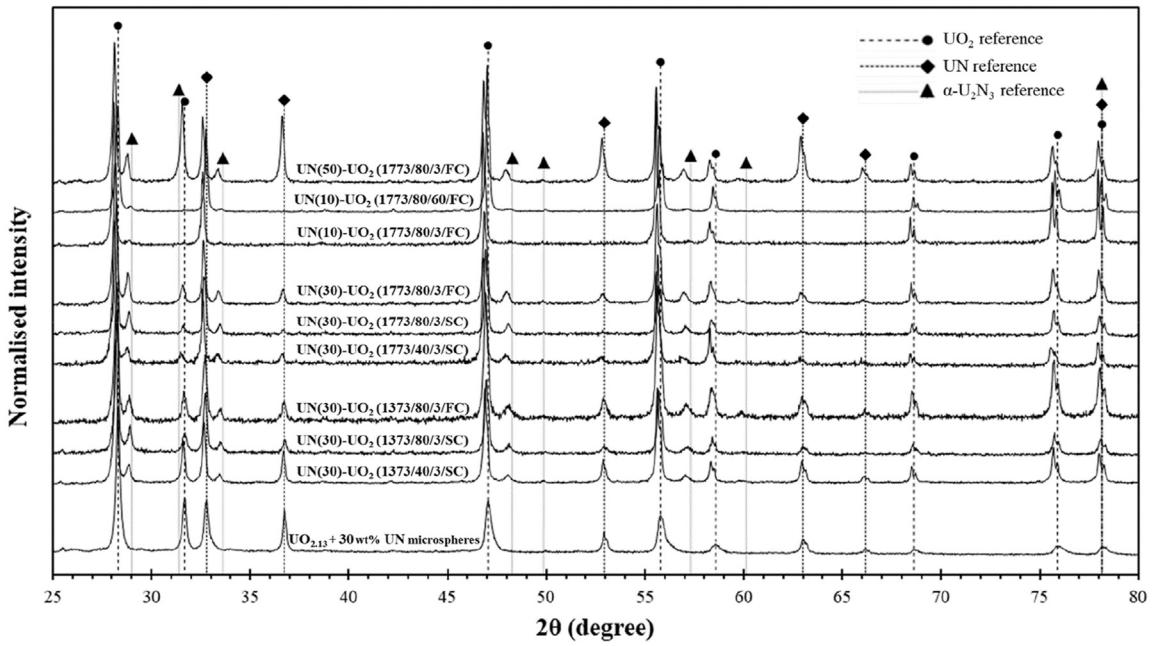

Fig. 10. X-ray diffraction patterns of mixed $UO_{2.13}$ and UN microspheres (30 wt%) powders before sintering (references), and UN-UO_2 composite fuels. Peaks related to the phase α-U_2N_3 (ICSD PDF 00-015-0426) are present in all sintered composite.

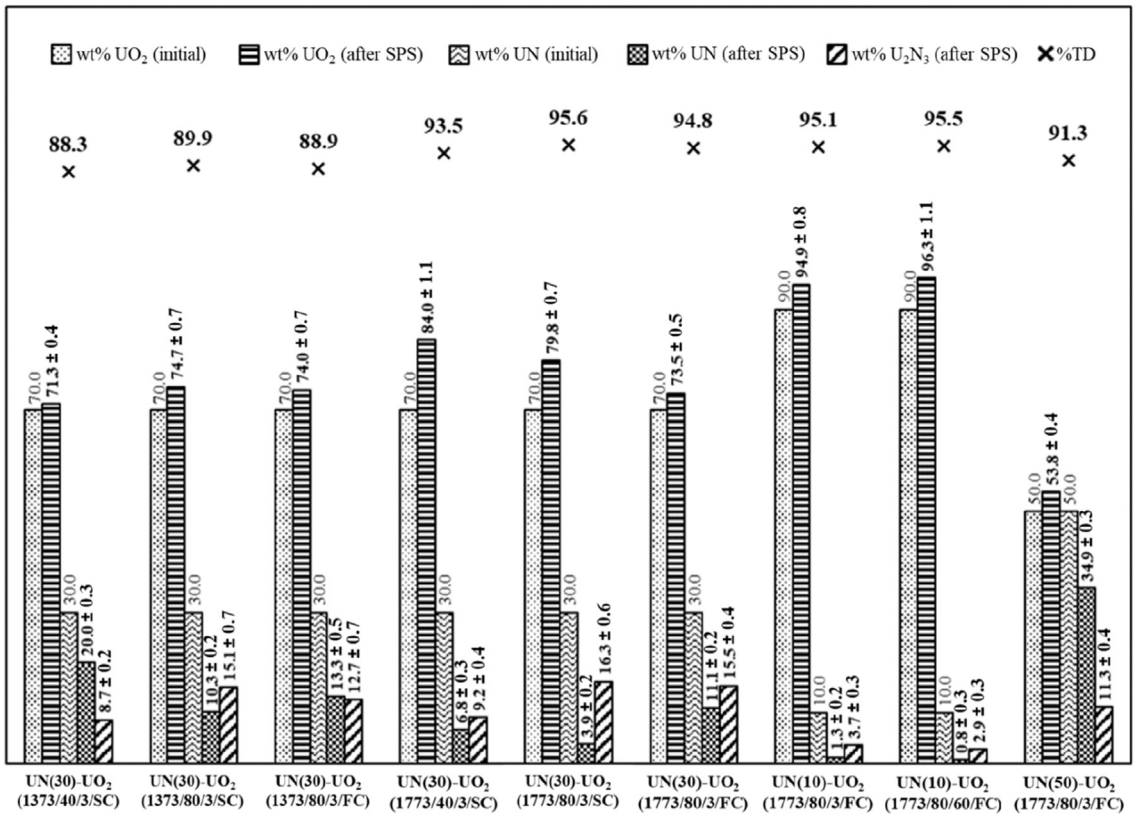

Fig. 11. Weight fractions of UO_2, UN and α-U_2N_3 before and after sintering derived by the Rietveld refinement method using the software MAUD [25], as well as the sintered densities of the composite fuels (%TD). Cooling rate and temperature affected the amount of phases and, consequently, the sintered densities. The faster the cooling or the lower the temperature, the lower the amount of α-U_2N_3.

microspheres, and the dotted line a new (and here called) diffusional interface. During heating, the oxygen from the $UO_{2.13}$ powder migrated towards the UN microsphere and interacted with the nitride phase, as demonstrated before (Figs. 4 and 6). This interaction resulted in a new oxide layer inside the UN microsphere, following the general behaviour: the higher the temperature, the

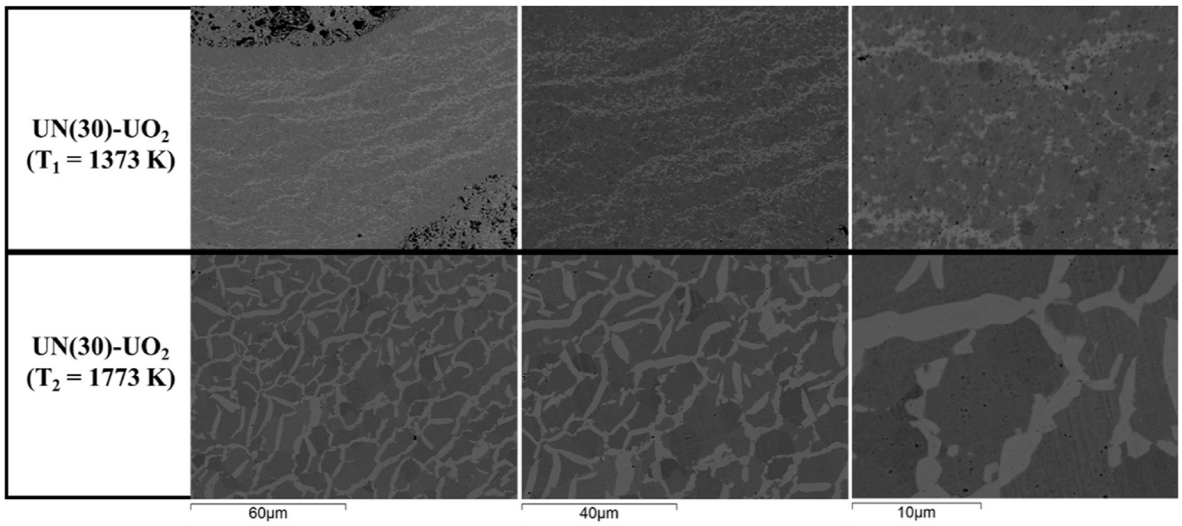

Fig. 12. Influence of the sintering temperature on the size and morphology of the precipitates (α-U_2N_3). Top and bottom images show samples UN(30)-UN (1373/80/3/SC) and UN(30)-UN (1773/80/3/SC) microstructures, respectively. Applied pressure, time and cooling rate (SC) were the same for both samples during the sintering. Higher temperature provided a bridged/connected lamellar-type precipitates, with average thickness of ~4 μm and ~15 μm long.

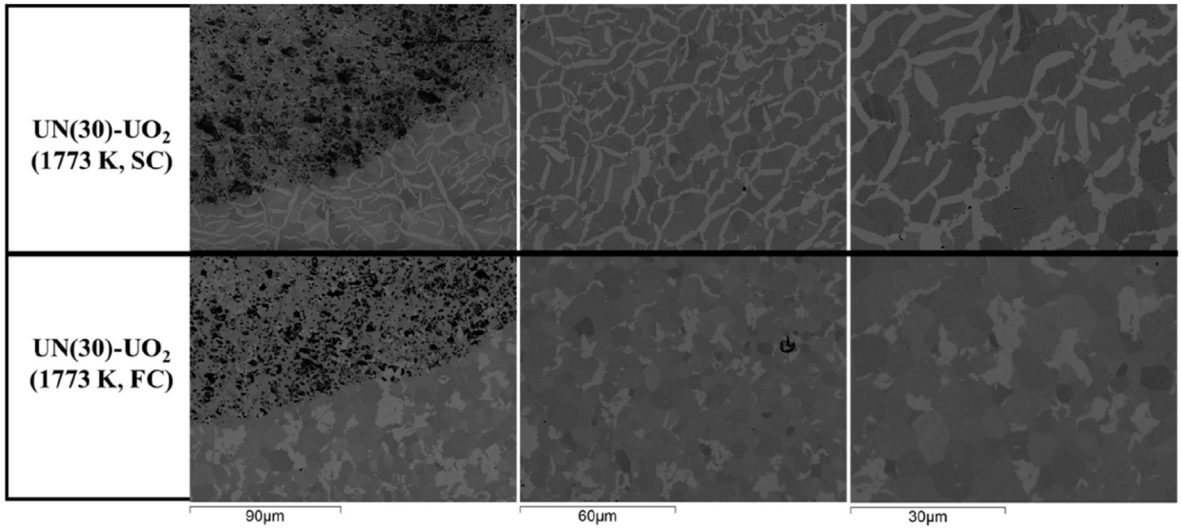

Fig. 13. Influence of the cooling rate on the size and morphology of the precipitates (α-U_2N_3). Top and bottom images show samples UN(30)-UN (1773/80/3/SC) and UN(30)-UN (1773/80/3/FC) microstructures, respectively. Temperature, time and applied pressure were the same for both samples during the sintering. Faster cooling rate (FC) formed coarse precipitates with various sizes (~5 μm−35 μm).

thicker the diffusional interface. The movement of the diffusional interface towards the centre of the UN microsphere acted as a driving force for the interdiffusion mechanism. Following the opposite direction, the nitrogen diffused into the oxide phase owing to the increase in the solubility of this element in the UO_2 matrix as a result of the increase in temperature [40]. Therefore, a long range solid solution such as $UO_{2-x}N_x$ could be formed, since the nitrogen stabilised the UO_{2-x} matrix after the mutual incorporation of O in UN and N in UO_{2-x}. The O diffused not only from the hyper-stoichiometry $UO_{2.13}$ powder, but also from the stoichiometric ($UO_{2.0}$) and hypo-stoichiometric phases (UO_{2-x}) [42]. Mishchenko's studies [22] corroborate this assumption, since precipitates were formed in sintered UN-UO_2 composites when stoichiometric $UO_{2.0}$ powder were used.

The precipitation mechanism is the second step to understand the formation of the sesquinitride phase. When the system reached the nominal sintering temperatures ($T_1 = 1373$ K and $T_2 = 1773$ K), a long range solid solution ($UO_{2-x}N_x$) could be formed. During the cooling, the solubility limit of N in UO_2 decreases and the nitrogen has to be redistributed from the (proposed) $UO_{2-x}N_x$ phase to the UO_2 matrix. This N redistribution, according to all the experimental results presented in this work, is the reason why the α-U_2N_3 phase formed in the UO_2 matrix. The slow cooling rates allowed the nitrogen to be redistributed in a long range (>600 μm) more uniformly during about e.g. 38 min (from 1773 K to 973 K), resulting in a lamellar-type microstructure (Fig. 13 top). Conversely, during the fast cooling, there was not enough time (e.g. 13 min from 1773 K to 973 K) for the nitrogen to be redistributed uniformly, which formed then a coarse precipitate structure (Fig. 13 bottom).

To better understand the precipitation phenomenon itself, EBSD grain orientation map was performed in sample UN(30)-UO_2 (1773/80/3/SC) (Fig. 16). The precipitation occurred along the UO_2 grain

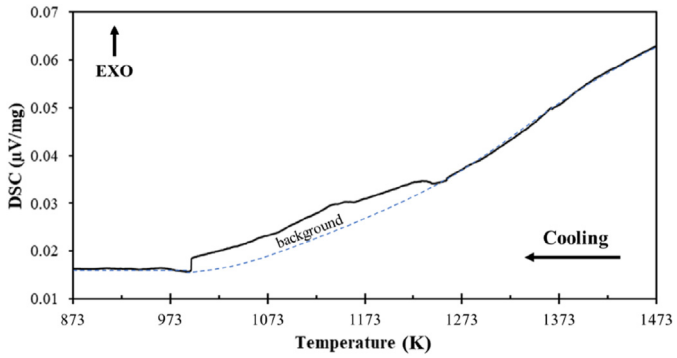

Fig. 14. Differential scanning calorimetry analysis of a UN(30)-UO_2 composite fuel during cooling (10 K/min). Exothermic peak (EXO) is pointed upwards from the background (dashed line). A broad exothermic peak may be observed between (about) 1253 K and 993 K, indicating that the N precipitation occurred within the temperature range of 1273 K–973 K.

boundaries and inside the UO_2 grains. A previous study also reported the formation of precipitates along the UO_2 grain boundaries, but did not discuss the precipitates inside the UO_2 grains [22]. As presented in Fig. 16, the phase precipitation mechanism seemed to follow, in some extend, specific crystallographic orientation patterns, including: i) spot 1 in Fig. 16 shows the green coloured α-U_2N_3 phase (110) coherently formed in UO_2 blue grains (111); ii) spot 2 in Fig. 16 shows the blue coloured α-U_2N_3 phase (111) precipitated in UO_2 red grains (001). Additionally, others coherent α-U_2N_3-UO_2 pattern colour pairs formed, such as beige-light blue (e.g. spot 3 in Fig. 16) and purple-green (e.g. spot 4 in Fig. 16). These preferential growths also corroborate with the proposed hypothesis of a precipitation mechanism occurring during cooling between 1273 K and 973 K, since the planes of atoms in the crystal structure of the precipitate were, in some extent, related to (or even coherent with) some specific planes in the crystal structure of the UO_2 matrix [39,43].

The interactions between UN and UO_2 during fabrication occur independent of the uranium nitride source, i.e. using either UN powder [10], or crushed UN sintered pellets (95–97 %TD) [22], or ~52 %TD UN microspheres (our study). Therefore, the interaction itself does not depend on the density/morphology/type of the UN phase.

4. Conclusions

A plausible formation mechanism of the α-U_2N_3 phase during the sintering of UN-UO_2 composite fuels was proposed. An innovative ATF concept was used: UN microspheres and $UO_{2.13}$ powder sintered by SPS. During the heating, the oxygen diffuses towards the UN microspheres and starts interacting with the nitride phase at (about) 1173 K. Simultaneously, the nitrogen diffuses into the UO_2 matrix and forms a long-range solid solution with the oxide phase, that can be described as $UO_{2-x}N_x$. The nitrogen stabilises the UO_{2-x} matrix after the mutual incorporation of O, from $UO_{2.13}$ and $UO_{2.0}$, in UN and N in UO_{2-x}. During the cooling, the solubility limit of N in $UO_{2-x}N_x$ decreases and, therefore, the nitrogen has to be redistributed from the $UO_{2-x}N_x$ phase. This N redistribution forms the α-U_2N_3 phase by a precipitation mechanism along and inside the UO_2 grains at temperatures between 1273 K and 973 K on cooling. Additionally, the SEM-EBSD results may indicate that the precipitation mechanism follows some specific crystallographic orientation patterns, including: the (110) and (111) α-U_2N_3 orientations seem to precipitate in the (111) and (001) UO_2 grain orientations, respectively. This correlation is reported for the first time here in this study.

In this paper we also demonstrated that temperature, pressure, and cooling rate considerably impacted the amount, size and morphology of the α-U_2N_3 phase. The following general behaviours are observed: the higher the temperature or the pressure, the lower the UN wt% and the higher the α-U_2N_3 wt%. Additionally, the temperature changes the morphology of the α-U_2N_3 precipitates: at 1373 K, the precipitates are small (~1–2 μm) and formless. Conversely, the ones at 1773 K have a quite oriented and interconnected lamellar-type structure (thickness of ~4 μm and ~15 μm long). The cooling rate impacts the amount, size and morphology of

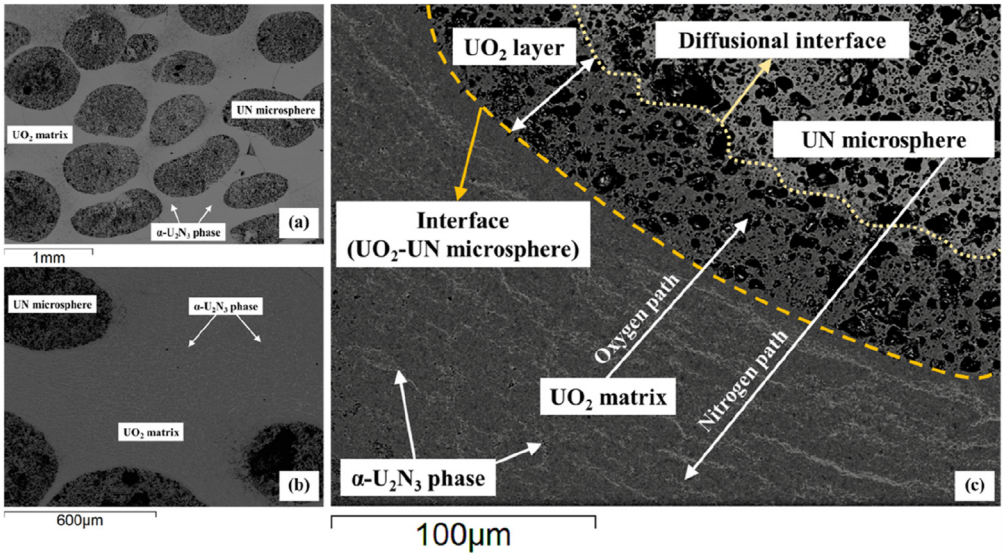

Fig. 15. SEM-BSE images of (a,b) low magnification UN microspheres embedded in UO_2 matrix, as well as indications of the α-U_2N_3 phase (brighter phase) spread throughout the pellet, and (c) sample UN(30)-UN (1373/80/3/SC), illustrating the proposed formation mechanism of α-U_2N_3 phase. The dashed line represents the original interface between the UO_2 matrix and the UN microsphere. The dotted line highlights a new interface between UO_2 and UN, called here diffusional interface. Additionally, the illustrative paths for the O and N migration, as well as the α-U_2N_3 precipitates are highlighted. The images indicate a long range diffusion of N towards the UO_2 matrix (>600 μm) and a formation of a UO_2 layer inside the UN microsphere as a result of the reaction between the O (from $UO_{2.13}$ and $UO_{2.0}$) and the UN.

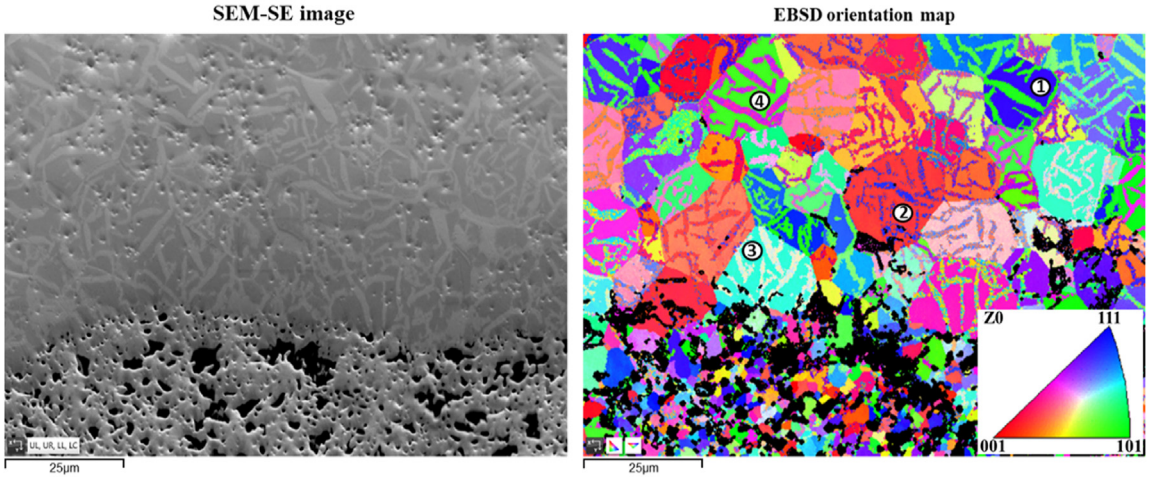

Fig. 16. SEM-SE image of the sample UN(30)-UO_2 (1773/80/3/SC) (left) and its EBSD orientation colour map (right) for UO_2 and α-U_2N_3 phases in the X direction, showing some coherent crystallographic precipitation patterns for the α-U_2N_3 phase in UO_2. Orientations (101) and (111) of α-U_2N_3 seemed to precipitate preferentially in UO_2 crystal orientations (111) and (001), e.g. spots 1 and 2, respectively. Additionally, e.g. spots 3 and 4 may show others coherent precipitation patterns. (For interpretation of the references to colour in this figure legend, the reader is referred to the Web version of this article.)

the precipitates as follow: the faster the cooling, the lower the amount of the sesquinitride phase. Moreover, slow cooling rates provide the formation of a long range lamellar-type structure. However, the fast cooling rates significantly changed the size and morphology of the precipitates: from a lamellar to a coarse grain structure (~5 μm−35 μm). The influences of temperature, pressure and cooling rate on the amount and morphology of the α-U_2N_3 phase are also for the first time studied and reported here.

In this study, we presented important, innovative and new achievements that may contribute to future studies on accident tolerant fuels. The SPS method has been shown to be quite effective to sinter a high density (~96 %TD) UN-UO_2 composite fuel in just 3 min (1773 K, 80 MPa). Furthermore, knowing the interaction between UN and UO_2, as well as the formation mechanism of the α-U_2N_3 phase, the amount of the undesirable sesquinitride phase may be minimised only by changing some SPS parameters. For instance, low temperature (<1173 K) and pressure, combined with a fast cooling rate, are quite effective to fabricate high density UN-UO_2 composite fuels with a maximised amount of UN. However, the UN will interact with the UO_2 at high temperatures (>1173 K) anyway, e.g. during operation in LWRs, and steps must be taken to avoid this interaction. Therefore, the findings in this paper may be a starting point for future developments of UN-UO_2 composite fuel as an accident tolerant fuel in LWR.

CRediT authorship contribution statement

Diogo Ribeiro Costa: Conceptualization, Methodology, Formal analysis, Investigation, Writing - original draft, Visualization. **Marcus Hedberg:** Investigation, Writing - review & editing. **Simon C. Middleburgh:** Conceptualization, Writing - review & editing, Supervision, Funding acquisition. **Janne Wallenius:** Conceptualization, Writing - review & editing, Supervision, Funding acquisition. **Pär Olsson:** Conceptualization, Resources, Supervision, Project administration, Funding acquisition. **Denise Adorno Lopes:** Methodology, Validation, Writing - review & editing, Supervision.

Declaration of competing interest

The authors declare that they have no known competing financial interests or personal relationships that could have appeared to influence the work reported in this paper.

Acknowledgments

Financial support from Swedish Foundation for Strategic Research (SSF, *Stiftelsen för Strategisk Forskning*) is acknowledged [Project reference number ID17-0078]. SCM is supported through the Sêr Cymru II programme funded through the Welsh European Funding Office (WEFO) under the European Regional Development Fund (ERDF). The authors wish to thank Dr. Mirva Eriksson, manager of National Facility of Spark Plasma Sintering (SPS) at Stockholm University, for the training and support during the SPS experiments. Also, we thank Dr. Jekabs Grins at Stockholm University for the DSC analyses, as well as Dr. Kjell Jansson at Stockholm University for the SEM-WDS examinations. Additionally, we wish to thank Dr. Joacim Hagström at Kista Swerim AB in Stockholm for the SEM-EDS/EBSD analyses and discussions.

Appendix A. Supplementary data

Supplementary data to this article can be found online at https://doi.org/10.1016/j.jnucmat.2020.152355.

References

[1] M. Pellegrini, K. Dolganov, L.E. Herranz, H. Bonneville, D. Luxat, M. Sonnenkalb, J. Ishikawa, J.H. Song, R.O. Gauntt, L.F. Moguel, F. Payot, Y. Nishi, Benchmark study of the accident at the Fukushima Daiichi NPS: best-estimate case, Nucl. Technol. 196 (2016) 198−210.
[2] B.R. Sehgal, Light water reactor (LWR) safety, Nucl. Eng. Technol. 38 (2006) 697−732.
[3] P.E. Evans, T.J. Davies, Uranium nitrides, J. Nucl. Mater. 10 (1963) 43−55.
[4] R.B. Matthews, Irradiation Performance of Nitride Fuels, Specialist Conference on Space Nuclear Power and Propulsion Technologies − Materials and Fuels, Podololsk-Moskow, Russia, 1993.
[5] J. Zakova, J. Wallenius, Fuel residence time in BWRs with nitride fuels, Ann. Nucl. Energy 47 (2012) 182−191.
[6] G.J. Youinou, R.S. Sen, Impact of accident-tolerant fuels and claddings on the overall fuel cycle: a preliminary systems analysis, Nucl. Technol. 188 (2014) 123−138.
[7] H. Zhao, D. Zhu, K.S. Chaudri, S. Qiu, W. Tian, G. Su, Preliminary transient thermal-hydraulic analysis for new coated UN and UC fuel options in SCWR, Prog. Nucl. Energy 71 (2014) 152−159.
[8] C. Ekberg, D.R. Costa, M. Hedberg, M. Jolkkonen, Nitride fuel for Gen IV nuclear power systems, J. Radioanal. Nucl. Chem. (2018), https://doi.org/10.1007/s10967-018-6316-0.
[9] B.J. Jaques, J. Watkins, J.R. Croteau, G.A. Alanko, B. Tyburska-Püschel, M. Meyer,

P. Xu, E.J. Lahoda, D.P. Butt, Synthesis and sintering of UN-UO_2 fuel composites, J. Nucl. Mater. 466 (2015) 745–754.
[10] J.H. Yang, D.-J. Kim, K.S. Kim, Y.-H. Koo, UO_2-UN composites with enhanced uranium density and thermal conductivity, J. Nucl. Mater. 465 (2015) 509–515.
[11] K.D. Johnson, J. Wallenius, M. Jolkkonen, A. Claisse, Spark plasma sintering and porosity studies of uranium nitride, J. Nucl. Mater. 473 (2016) 13–17.
[12] G.A. Rama Rao, S.K. Mukerjee, V.N. Vaidya, V. Venugopal, D.D. Sood, J. Nucl. Mater. 185 (1991) 231–241.
[13] K. Johnson, V. Ström, J. Wallenius, D.A. Lopes, Oxidation of accident tolerant fuel candidates, J. Nucl. Sci. Technol. 54 (2017) 280–286, https://doi.org/10.1080/00223131.2016.1262297.
[14] D.A. Lopes, S. Uygur, K. Johnson, Degradation of UN and UN–U_3Si_2 pellets in steam environment, J. Nucl. Sci. Technol. 54 (2017) 405–413, https://doi.org/10.1080/00223131.2016.1274689.
[15] M. Jolkkonen, P. Malkki, K. Johnson, J. Wallenius, Uranium nitride fuels in superheated steam, J. Nucl. Sci. Technol. 54 (2017) 513–519, https://doi.org/10.1080/00223131.2017.1291372.
[16] J.K. Watkins, D.P. Butt, B.J. Jaques, Microstructural degradation of UN and UN-UO_2 composites in hydrothermal oxidation conditions, J. Nucl. Mater. 518 (2019) 30–40.
[17] E.L. Bright, S. Rennie, A. Siberry, K. Samani, K. Clarke, D.T. Goddard, R. Springell, Comparing the corrosion of uranium nitride and uranium dioxide surfaces with H_2O_2, J. Nucl. Mater. 518 (2019) 202–207.
[18] P.A. Lessing, Oxidation Protection of Uranium Nitride Fuel Using Liquid Phase Sintering, INL/EXT-12-24974, 2012, https://doi.org/10.2172/1036778 technical report, INL.
[19] P. Malkki, The Manufacturing of Uranium Nitride for Possible Use in Light Water Reactors, Licentiate thesis, KTH Royal Institute of Technology, Stockholm, Sweden, 2015, https://www.diva-portal.org/smash/get/diva2:816319/FULLTEXT01.pdf.
[20] K.D. Johnson, A.M. Raftery, D.A. Lopes, J. Wallenius, Fabrication and microstructural analysis of UN-U_3Si_2 composites for accident tolerant fuel applications, J. Nucl. Mater. 477 (2016) 18–23.
[21] L.H. Ortega, B.J. Blamer, J.A. Evans, S.M. McDeavitt, Development of an accident-tolerant fuel composite from uranium mononitride (UN) and uranium sesquisilicide (U_3Si_2) with increased uranium loading, J. Nucl. Mater. 471 (2016) 116–121.
[22] Y. Mishchenko, Composite UN-UO_2 Fuels, Master Thesis in Nuclear Energy Engineering, KTH Royal Institute of Technology, Stockholm, Sweden, 2018. http://www.diva-portal.se/smash/get/diva2:1252197/FULLTEXT01.pdf.
[23] A.P. Shivprasad, A.C. Telles, J.T. White, Report on Waterproofing of UN Studies, LA-UR-19-28422, Nuclear Technology Research and Development, Los Alamos National Laboratory, 2019.
[24] R.B. Matthews, K.M. Chidester, C.W. Hoth, R.E. Mason, R.L. Petty, Fabrication and testing of uranium nitride fuel for space power reactors, J. Nucl. Mater. 151 (1988) 334–344.
[25] L. Lutterotti, M. Bortolotti, G. Ischia, I. Lonardelli, H.-R. Wenk, Rietveld texture analysis from diffraction images, Z. Kristallogr. (Suppl. 26) (2007) 125–130.
[26] R.E. Rundle, A.S. Wilson, N.C. Baenziger, R.A. McDonald, The structures of the carbides, nitrides and oxides of uranium, J. Am. Chem. Soc. 70 (1948) 99–105.
[27] M.-C. Lee, C.-J. Wu, Conversion of UF_6 to UO_2: a quasi-optimization of the ammonium uranyl carbonate process, J. Nucl. Mater. 185 (1991) 190–201.
[28] M. Durazzo, A.M. Saliba-Silva, E.F. Urano de Carvalho, H.G. Riella, Sintering behavior of UO_2-Gd_2O_3 fuel: pore formation mechanism, J. Nucl. Mater. 433 (2013) 334–340.
[29] L. Ge, G. Subhash, R.H. Baney, J.S. Tulenko, E. McKenna, Densification of uranium dioxide fuel pellets prepared by spark plasma sintering (SPS), J. Nucl. Mater. 435 (2013) 1–9.
[30] M. Durazzo, A.C. Freitas, A.E.S. Sansone, N.A.M. Ferreira, E.F. Urano de Carvalho, H.G. Riella, R.M.L. Neto, Sintering behavior of UO_2-Er_2O_3 mixed fuel, J. Nucl. Mater. 510 (2018) 603–612.
[31] R.M. German, Sintering: from Empirical Observations to Scientific Principles, first ed., Butterworth-Heinemann, Oxford, 2014.
[32] K.S. Kim, G.M. Kim, K.W. Song, J.H. Yang, K.W. Kang, Y.H. Jung, Sintering behavior of Cr_2O_3-doped UO_2 pellets, J. Korean Nucl. Soc. 35 (2003) 14–24.
[33] V. Peres, L. Favergeon, M. Andrieu, J.C. Palussière, J. Balland, C. Delafoy, M. Pijolat, High temperature chromium volatilization from Cr_2O_3 powder and Cr_2O_3-doped UO_2 pellets in reducing atmospheres, J. Nucl. Mater. 423 (2012) 93–101.
[34] G.H. Price, W.I. Stuart, Thermal Decomposition of Ammonium Uranates, Australian Atomic Energy Commission, AASC/E276, 1973, ISBN 0 642 99555 9.
[35] L. Ge, G. Subhasha, R.H. Baney, J.S. Tulenko, Influence of processing parameters on thermal conductivity of uranium dioxide pellets prepared by spark plasma sintering, J. Eur. Ceram. Soc. 34 (2014) 1791–1801.
[36] P. Cavaliere, Spark Plasma Sintering of Materials: Advances in Processing and Applications, Springer Nature, Switzerland, 2019, https://doi.org/10.1007/978-3-030-05327-7.
[37] O. Guillon, J. Gonzalez-Julian, B. Dargatz, T. Kessel, G. Schierning, J. Räthel, M. Herrmann, Field-assisted sintering technology/spark plasma sintering: mechanisms, materials, and technology developments, Adv. Eng. Mater. (2014), https://doi.org/10.1002/adem.201300409.
[38] D.R. Costa, A.C. Freitas, Thermal stability test of UO_2-doped pellet manufactured at INB, in: International Nuclear Atlantic Conference - INAC 2017, *Associação Brasileira de Energia Nuclear* – ABEN, Belo Horizonte, MG, Brazil, 2017, ISBN 978-85-99141-07-6.
[39] R.E. Smallman, A.H.W. Ngan, Modern Physical Metallurgy, eighth ed., Elsevier, Oxford, 2014.
[40] H. Tagawa, Phase relations and thermodynamic properties of the uranium-nitrogen system, J. Nucl. Mater. 51 (1974) 78–89.
[41] S. Vyazovkin, N. Koga, C. Schick, Handbook of Thermal Analysis and Calorimetry: Recent Advances, Techniques and Applications, second ed., Elsevier, 2018, ISBN 9780444640635 vol. 6.
[42] K.C. Kim, D.R. Olander, Oxygen diffusion in UO_{2-x}, J. Nucl. Mater. 102 (1981) 192–199.
[43] D.R. Askeland, P.P. Fulay, D.K. Bhattacharya, Essentials of Materials Science & Engineering - SI Version, second ed., CENGAGE Learning, Stamford, 2010. EUA.